A Novel Quasi-Resonant Battery Charger for Photovoltaic Applications

(Article begins on next page)

16 May 2024

A Novel Quasi-Resonant Battery Charger for Photovoltaic Applications

Stefano Cerutti, Francesco Musolino, Paolo S. Crovetti

Department of Electronics and Telecommunications

Politecnico di Torino

Torino, Italy

{stefano.cerutti, francesco.musolino, paolo.crovetti}@polito.it

Abstract—**This work presents the analysis, design, PCB implementation and testing of a quasi-resonant low-voltage battery charger intended to be supplied by a photovoltaic (PV) module. The proposed battery charger exploits the Discontinuous Voltage Mode operation to transfer to the load a controlled and discrete amount of energy, alternately stored and released by two half-bridge capacitors. A small resonant inductance is added to assist the soft commutation of all the converter MOSFETs. The mathematical description of the operating principle and the main design equations of the converter are reported. Based on experiments, a 100 W prototype of the proposed battery charger achieves a flat conversion efficiency higher than 92 % over the wide 20 W − 95 W power range, with a peak of nearly 94 % at 40 W.**

Index Terms—**Quasi-resonant converter, battery charger, photovoltaic, soft-switching, Zero-Voltage Switching.**

I. INTRODUCTION

Sustainable Development Goal (SDG) 7 of the 2030 Agenda of the United Nations, by promoting the extension of affordable, reliable and sustainable energy systems, addresses the need to increase the Renewable Energy Sources (RES) inside the countries energy mix [1]. Beside generation, a consistent effort should be devoted to more reliable and efficient conversion and distribution systems. Among the photovoltaic (PV)-fed applications, increasing attention is devoted to battery charging, especially for stand-alone systems [2]. Battery chargers for PV-fed applications should be designed to achieve a high efficiency over a wide range of operating powers, to address the intrinsic variability of RES.

To achieve a high efficiency conversion, resonant power converters have become a promising alternative to conventional Pulse-Width Modulated (PWM) converters, thanks to the possibility to reduce or eliminate the switching losses, reduce the Electromagnetic Interference (EMI) and increase the power density [3].

While extensive attention is devoted to resonant power converters for photovoltaic-to-grid applications [4], fewer works are devoted to resonant PV-fed low-voltage battery chargers. Most of the low-voltage battery chargers exhibit buck-derived topologies endowed with auxiliary resonant networks to achieve the soft commutation of their switches. The quasi-resonant buck-derived converter in [5] includes an additional LC resonant network to achieve the Zero-Voltage Switching (ZVS) of the main MOSFET. However, a resonant peak across

the main MOSFET requires to double its voltage rating, and the measured peak and average charging efficiencies of the proposed converter are 87 % and 84 % respectively. Another buck-derived topology is presented in [6], which achieves the Zero-Current Switching (ZCS) turn-OFF of the main switch thanks to an additional LC tank and an auxiliary switch. However, the large current peak on the input MOSFET, the large voltage peak on the output diode and the 90.3 % peak efficiency remain the main issues of this converter. A PV-fed dual-stage converter is presented in [7], where a PWM boost-stage responsible for the Maximum Power-Point Tracking (MPPT) is followed by a half-bridge parallel-loaded resonant converter. Despite the desirable integration of MPPT, the relatively large component count and the adoption of a passive full-bridge rectifier results in a 88.7 % average and 92 % peak charging efficiency.

Aiming to achieve high conversion efficiency over a wide power range, a new PV-fed quasi-resonant converter is presented in this work. The topology is based on the grid-supplied constant power charger previously proposed in [8], but modified and optimized for a PV source. Differently from the above-mentioned topologies, the converter presented here exploits the parasitic capacitances of its switches to obtain soft commutation with an increase in power density. The rest of the paper is organized as follows: Section II describes the topology and operation of the converter. In Section III, the design of the converter is discussed in details. In order to validate the proposed approach, a 100 W prototype is built and the experimental results are presented in Section IV, while Section V draws the conclusions of this work.

II. ANALYSIS

A. Operating principle

This work explores the possibility to apply the operating principle adopted in the constant-power charger described in [8] to a different topology optimized for a PV-sourced application. The topology, illustrated in Fig. 1, consists in a quasi-resonant, frequency-modulated half-bridge inverting stage (MOSFETs M_1 and M_2 and capacitors C_1 and C_2, with $C_1 = C_2 = C$) followed by an active rectifier stage.

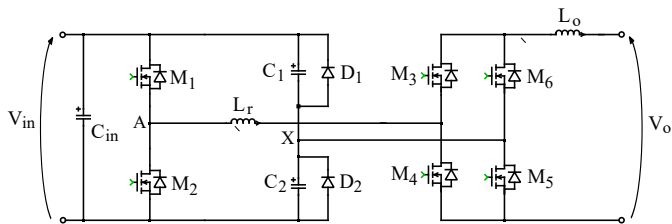The input MOSFETs are controlled with $180°$ phase shift and nearly 50% duty cycle, so as to generate a pure AC

Fig. 1: Proposed quasi-resonant battery charger.

voltage between nodes A and X. Unlike conventional half-bridge converters, in which the capacitances are selected to be large enough to maintain a stable voltage at node X, C_1 and C_2 are designed here to be alternately charged and discharged between $0\,\mathrm{V}$ and the input voltage. The output current is responsible for the charge and discharge of the half-bridge capacitances.

Clamping diodes D_1 and D_2 are added in anti-parallel connection to avoid charging C_1 and C_2 above V_{in} or discharging them below $0\,\mathrm{V}$. This principle, denoted in [8] by Discontinuous Voltage Mode (DVM), allows to generate a triangular voltage across each capacitor and to transfer to the output a discretized amount of energy at each switching cycle.

An input capacitor C_{in} is added to the input port to stabilize the working point of the PV module.

The step-down transformer originally present in the grid-fed topology in [8] is here removed because of the lower input voltage of the targeted PV-fed application. A typical crystalline-Silicon PV module (with 48 up to 72 cells), indeed, exhibits Maximum Power Point voltages (V_{MPP}) around few tens of volts, which do not need significant step-down to the low-voltage batteries.

An active rectifier, consisting of MOSFETs M_3, M_4, M_5 and M_6, provides a full-wave rectification of the intermediate AC voltage. The choice of an active rectifier, despite the additional gate driving complexity, allows to eliminate the forward voltage drops of a passive diode-based rectifier. By considering, for instance, a $12\,\mathrm{V}$ battery and Schottky diodes with $0.4\,\mathrm{V}$ forward voltage, indeed, the diode conduction losses alone would imply almost $7\,\%$ efficiency loss. Low $R_{\mathrm{DS,ON}}$ transistors are required to limit the influence of conduction losses on the conversion efficiency.

The additional small resonant inductor L_{r}, connected to the switching node A between the half-bridge MOSFETs, is specifically added to assist the ZVS turn-ON of M_1 and M_2.

An inductor L_{o} filters the high-frequency harmonics of the output current I_{o} to provide a smooth charging of the output battery.

B. Analysis of a switching cycle

This section provides the analysis of the main converter voltage and current waveforms through a switching period. Since the operation of the converter is symmetric, the description only considers a half period.

The mathematical analysis of a switching period presented here is based on the following assumptions:

- the input capacitor C_{in} is assumed to keep a constant DC input voltage V_{in};
- the output filter inductor L_{o} is assumed to keep a constant DC output current I_{o};
- the half-bridge MOSFETs M_1 and M_2 are ideal, except for their output parasitic capacitance C_{s};
- the forward voltage drops of the clamping diodes and MOSFETs body diodes are neglected;
- the reactive components C_1, C_2, L_{r} and L_{o} are lossless and ideal.

The working operation of the converter in a half switching period can be subdivided into 3 phases that are illustrated in Fig. 2.

1) Power transfer phase (PT, Fig. 2a): During this phase, M_1, M_3 and M_5 conduct the output current I_{o}, whereas M_2, M_4 and M_6 are turned OFF. At node X, I_{o} splits equally, gradually charging C_2 and discharging C_1. V_{x} increases linearly from $0\,\mathrm{V}$ to V_{in}, as shown in Fig. 3:

$$V_{\mathrm{x}}(t) = \frac{I_{\mathrm{o}}}{2C}t. \qquad (1)$$

During this phase, L_{r} is connected in series to L_{o}. As a consequence, since I_{o} is assumed to be constant, no voltage drop appears across it. The rectifier primary voltage V_{p} assumes a triangular behaviour:

$$V_{\mathrm{p}}(t) \approx V_{\mathrm{A}} - V_{\mathrm{x}} = V_{\mathrm{in}} - \frac{I_{\mathrm{o}}}{2C}t. \qquad (2)$$

The secondary voltage V_{s} temporarily coincides with V_{p}. This phase ends when V_{x} has reached V_{in}.

2) Current circulating phase (CC, Fig. 2b): M_1, M_3 and M_5 are still ON. When V_{x} has reached V_{in}, the bypass diode D_1 gets forward biased and clamps V_{x}, as shown in Fig. 3. The rectifier primary voltage V_{p} becomes zero and forces the body diodes of M_4 and M_6 to turn-ON, which start sinking current from M_3 and M_4. A free-wheeling path for I_{o} is created and no power is temporarily transferred to the battery.

3) Crossover resonant phase (CR, Fig. 2c-2e): This phase begins when M_1 is turned OFF. During the dead-time, L_{r} starts resonating with the output parasitic capacitances of M_1 and M_2 ($C_{\mathrm{s1}} = C_{\mathrm{s2}} = C_{\mathrm{s}}$), as shown in Fig. 2c, pushing V_{A} below $0\,\mathrm{V}$, as illustrated in Fig. 3. This behaviour only occurs if the energy stored in the tank inductor L_{r} is sufficient to completely charge C_{s1}. This condition translates into a lower boundary for L_{r}:

$$L_{\mathrm{r}} > \frac{2C_{\mathrm{s}}V_{\mathrm{in}}^2}{I_{\mathrm{o}}^2}. \qquad (3)$$

Once V_{A} reaches $0\,\mathrm{V}$, the body diode of M_2 gets forward-biased and conducts the L_{r} current $i_{\mathrm{L_r}}$, as shown in Fig. 2d. The voltage V_{x} (almost constant during this phase) appears across L_{r} and forces $i_{\mathrm{L_r}}$ to a linear decrease:

$$i_{\mathrm{L_r}} = I_o - \frac{V_{\mathrm{in}}}{L_{\mathrm{r}}}t. \qquad (4)$$

The difference between $i_{\mathrm{L_r}}$ and I_{o} flows through the body diodes of M_4 and M_6.
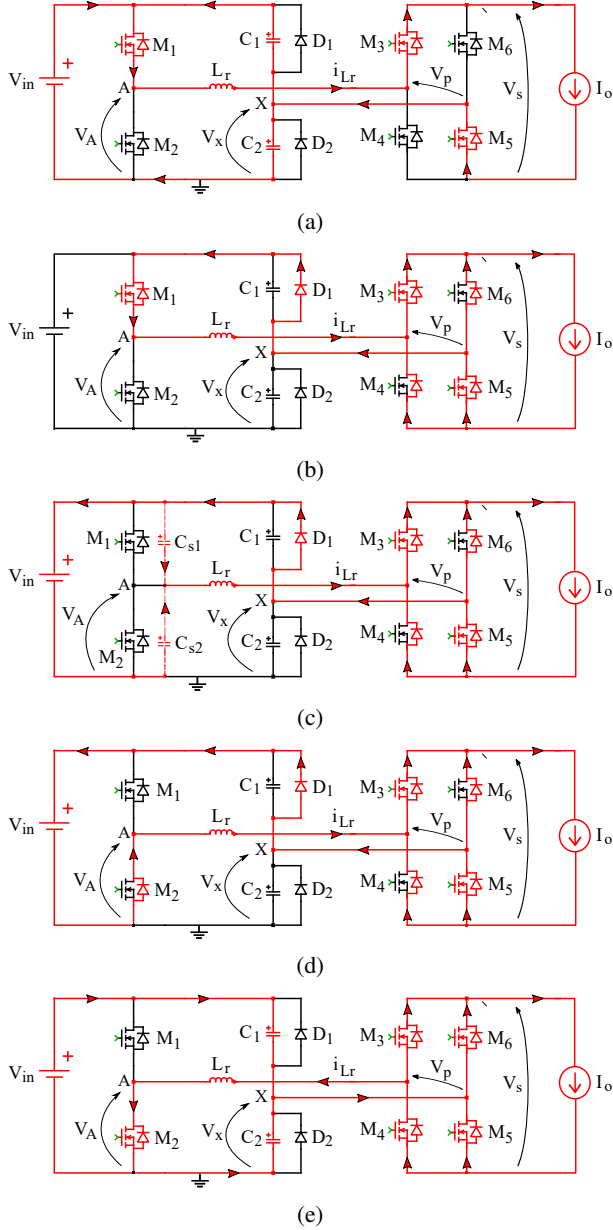
Fig. 2: Operation of the converter during a half switching period: (a) PT phase; (b) CC phase; (c) CR phase: L_r resonates with C_{s1} and C_{s2}; (d) CR phase: the body diode of M_2 starts conducting; (e) CR phase: M_2, M_4 and M_6 turn-ON at zero voltage, and i_{L_r} inverts its polarity.

Fig. 3: Main voltage and current waveforms in a switching period.

After a deadtime t_{dead}, M_2 is turned ON, as shown in Fig. 2e. If its body diode is still conducting, the commutation occurs at zero voltage, as schematically represented in Fig. 3. In this case, the energy stored in the parasitic capacitance of the turned-OFF MOSFET, instead of being dissipated, is recovered at the input. The maximum allowed deadtime $t_{dead,max}$ to achieve ZVS is limited by the time required by the parasitic output capacitance C_{s2} of M_2 to be fully discharged (denoted by t_1), and by i_{L_r} to become null: when it inverts its polarity, indeed, L_r starts resonating again with the output
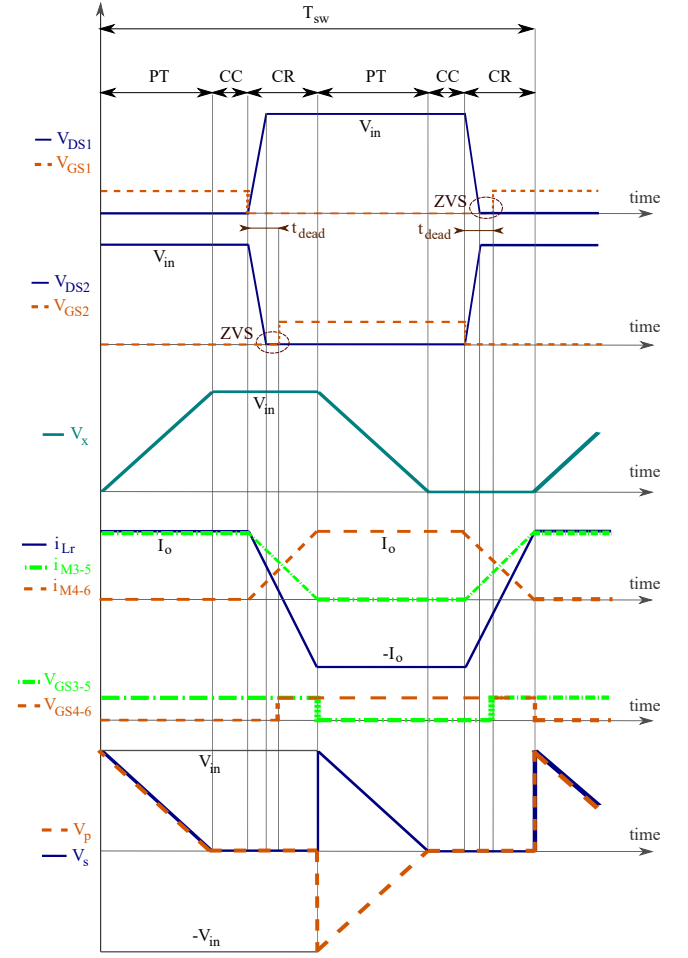
capacitances of M_1 and M_2, and the ZVS condition is lost. This maximum time can be analytically estimated assuming a linear current discharge:

$$t_{dead,max} \approx t_1 + \frac{L_r I_o}{V_{in}} \, . \tag{5}$$

Together with M_2, also M_4 and M_6 are turned ON, at zero-voltage. The Kirchhoff Current Law (KCL) applied at the output nodes allows to derive the source-to-drain MOSFETs currents as:

$$i_{M_3} = i_{M_5} = \frac{I_o}{2} + \frac{i_{L_r}}{2} \tag{6}$$

$$i_{M_4} = i_{M_6} = \frac{I_o}{2} - \frac{i_{L_r}}{2} \, . \tag{7}$$

From (6), if M_3 and M_5 are turned OFF when $i_{L_r} = -I_o$, ZCS commutation is achieved, as shown in Fig. 3. The CR phase is concluded when M_3 and M_5 are turned OFF. It is important to observe that the duration of this phase is exaggerated in Fig. 3 for a better visualization.

The previous analysis assumes that the switching period is long enough to allow I_o charging and discharging C_1 and C_2

between $0\,\mathrm{V}$ and V_{in}. If this is true, the transferred power can be simply computed by multiplying the energy stored and released by each capacitor C_1 and C_2 by the switching frequency:

$$P \approx 2C V_{\mathrm{in}}^2 f_{\mathrm{sw}}. \qquad (8)$$

However, this condition occurs only if I_{o} can raise/lower the V_x voltage by V_{in}. Given a target peak current $I_{\mathrm{o,max}}$, the condition holds for:

$$\frac{T_{\mathrm{sw}}}{2} \geq 2C \frac{V_{\mathrm{in}}}{I_{\mathrm{o,max}}} \Rightarrow f_{\mathrm{sw}} \leq \frac{I_{\mathrm{o,max}}}{4C V_{\mathrm{in}}} \triangleq f_{\mathrm{limit}}. \qquad (9)$$

For $f_{\mathrm{sw}} > f_{\mathrm{limit}}$, the output power starts decreasing non-linearly with the switching frequency. In this second operating mode, I_{o} charges and discharges only partially C_1 and C_2, causing D_1 and D_2 to never enter in conduction. As a result, V_x assumes a triangular shape centered around $V_{\mathrm{in}}/2$ and the CC phase is not achieved.

Beside this, the PT and CR operating phases remain as before. Due to the partial charging of the dividing capacitors, V_{p} and V_{s} assume a trapezoidal behaviour.

It is important to observe that the battery charging voltage is the average of V_{s}, which is a direct consequence of the volt-second balance applied to L_{o}. This implies that, to ensure the desired battery charging:

$$\overline{V_{\mathrm{s}}} \approx \frac{V_{\mathrm{in}}}{2} \geq V_{\mathrm{batt}} \Rightarrow V_{\mathrm{in}} \geq \frac{V_{\mathrm{batt}}}{2}. \qquad (10)$$

Condition (10) dictates the minimum input voltage, i.e. the minimum number of series-connected cells that the input PV source should exhibit to satisfy the voltage constraint. Assuming monocrystalline silicon, a good estimate for the open circuit voltage is $0.55\,\mathrm{V}$ [9]: as such, a minimum number of 48 cells is required to ensure net power flow to a $12\,\mathrm{V}$ battery.

III. DESIGN OF A 100 W PROTOTYPE

A physical prototype was designed and tested to validate the predicted theoretical and simulation results on the working operation, and to derive the converter performances in terms of conversion efficiency. The designed input voltage was selected to be below $30\,\mathrm{V}$, corresponding to typical open-circuit voltages of 48-cell PV panels.

The converter MOSFETs exhibit the same current stresses ($I_{\mathrm{o}}/2$ RMS current and I_{o} peak current), but different voltage stresses. While M_1 and M_2 voltage is bounded by V_{in}, the rectifier MOSFETs are subjected to large voltage spikes when they are turned OFF. This phenomenon occurs because the difference between $i_{L_{\mathrm{r}}}$ and I_{o} flows in their parasitic capacitances, producing resonant spikes that require to increase their voltage rating. Due to the temporary shortage of silicon power devices, the same $100\,\mathrm{V}$ rated transistor was selected. Since the topology is designed to reduce or eliminate the switching losses, a low conduction resistance $R_{\mathrm{DS,ON}}$ (below $10\,\mathrm{m\Omega}$) is determinant to obtain a high-efficiency conversion.

The adopted Si-MOSFETs, can be turned ON with $V_{\mathrm{GS}} = 5\,\mathrm{V}$. A dual-output DC-DC converter was adopted to generate the supply voltages for the half-bridge and rectifier MOSFETs from V_{in}. Three half-bridge gate drivers were selected, which rely on external bootstrap networks to drive the high-side MOSFETs.

The dividing capacitors C_1 and C_2 are subjected to a significant RMS current stress $\frac{I_{\mathrm{o}}}{2}$, requiring a low ESR and large stability to frequency variations. On the other hand, their working voltage is limited by V_{in}, thanks to the clamping diodes action. The capacitance value is a design parameter linked to the desired rated power, at rated source voltage and boundary frequency conditions, as determined in Eq. (9). In the present design, assuming $100\,\mathrm{W}$ rated power at $28\,\mathrm{V}$ input voltage, $12\,\mathrm{V}$ battery voltage and $60\,\mathrm{kHz}$ operation, the required capacitance must satisfy:

$$C \leq \frac{P_{\mathrm{rated}}}{4 f_{\mathrm{limit}} V_{\mathrm{in}} V_{\mathrm{batt}}} \approx 1.24\,\mathrm{\mu F}. \qquad (11)$$

The adopted Multi-Layer Ceramic Capacitor (MLCC) is characterized by $50\,\mathrm{V_{DC}}$ rated voltage, $12\,\mathrm{A_{RMS}}$ rated current at $100\,\mathrm{kHz}$ and $940\,\mathrm{nF}$ capacitance.

The input capacitor C_{in}, responsible for stabilizing the working point of the PV panel was selected according to the allowed input current ripple. This limit can be linked to the deterioration of the output power of a PV panel when it is forced to provide strongly rippled current.

Elkhateb et al. in [10], exploiting a Single-Diode Model (SDM), derived an analytic relation between the current ripple ΔI_{RMS} and the power decrease $\Delta P_{\mathrm{ripple}}$ of a PV panel:

$$\frac{\Delta P_{\mathrm{ripple}}}{P_{\mathrm{MPP}}} \approx 10.67 \left(\frac{\Delta I_{\mathrm{RMS}}}{I_{\mathrm{MPP}}}\right)^2. \qquad (12)$$

By applying this approach to the equivalent SDM of a commercial poly-crystalline silicon 48-cell, an approximated constraint was derived for the capacitor ESR:

$$ESR \ll 650\,\mathrm{m\Omega}. \qquad (13)$$

From the relation of the RMS currents applied at the input node, an approximated expression for the RMS capacitor current $i_{\mathrm{C_{in,RMS}}}$ can be derived:

$$i_{\mathrm{C_{in,RMS}}} \approx 2C f_{\mathrm{sw}}(V_{\mathrm{in}} + 2V_{\mathrm{fd}})\sqrt{\frac{V_{\mathrm{in}}}{2V_{\mathrm{batt}}} - 1}, \qquad (14)$$

where V_{fd} is the forward voltage drop of the clamping diodes. Assuming the above-mentioned worst-case conditions, $i_{\mathrm{C_{in,RMS}}} \approx 1.34\,\mathrm{A}$. An aluminum electrolytic capacitor was selected, exhibiting $63\,\mathrm{V}$ rated voltage, $750\,\mathrm{\mu F}$ capacitance, $68\,\mathrm{m\Omega}$ ESR and $2.5\,\mathrm{A}$ rated ripple current.

The inductor L_{o} was sized according to the maximum allowed current ripple overimposed to the average charging current. Application Notes like [11] recommend to limit the ripple current in *ampere* below a value equal to $1/20$ of

the battery capacity, expressed in *ampere-hour*. Considering a $50\,\mathrm{A\,h}$ battery, for instance, the ripple current should be maintained below $2.5\,\mathrm{A}$.

By integrating the L_o voltage, an approximated value of the parabolic current ripple can be determined:

$$\Delta I_\mathrm{o,ripple} \approx \frac{V_\mathrm{in}}{12 f_\mathrm{sw} L_\mathrm{o}} < 2.5\,\mathrm{A}\,. \qquad (15)$$

The current rating should consider the maximum charging current ($\approx 8\,\mathrm{A}$ for a $100\,\mathrm{W}$ operation). A ferrite-core, wire-wound inductor was selected, with $8.8\,\mathrm{m\Omega}$ DC resistance, $13\,\mathrm{A}$ saturation current for 30% inductance decrease, and $17.5\,\mathrm{A}$ maximum current for a temperature increase of $40\,^\circ\mathrm{C}$. Its $47\,\mathrm{\mu H}$ inductance satisfies Eq. (15) for the rated power condition. The DC losses of this component at the maximum power condition are estimated to weigh for around the 0.6% of the total power.

The inductance value of L_r, investigated in details in this work, determines two concurrent consequences:
- the maximum allowed deadtime to achieve ZVS of the half-bridge MOSFETs, as described in (3). L_r should be large enough to relax the timing constraints imposed on the controller and the gate drivers;
- on the other hand, an increased inductance value increases the reactive power absorbed by L_r, in turns decreasing the power peak of the static characteristic and reducing f_limit.

A trade-off value of $330\,\mathrm{nH}$ was selected iteratively relying on *LTspice XVII* simulations [12]. According to (3), this value, combined with the MOSFETs parasitic $C_\mathrm{s} = 640\,\mathrm{pF}$ and with $V_\mathrm{in} = 28\,\mathrm{V}$, satisfies the necessary condition for ZVS for any output current larger than $1.23\,\mathrm{A}$. This consideration has important consequences on the behaviour of the conversion efficiency: it states that L_r value provides a minimum operating power above which a deadtime exists such that ZVS can be achieved. As a result, the switching losses, which may be impactful at light loads conditions, are basically eliminated on a wide range of larger operating powers, if a proper deadtime is selected. It is meaningful to observe that the ZVS condition is achieved exploiting a small inductor and the output parasitic capacitances of the half-bridge MOSFETs, with benefits on the power density.

A ferrite-core inductor was selected, exhibiting low DC resistance ($1.3\,\mathrm{m\Omega}$), $36.5\,\mathrm{A}$ rated current for $40\,^\circ\mathrm{C}$ temperature increase, and $62\,\mathrm{A}$ saturation current for a 20% inductance decrease.

Tab. I summarizes the selected components for the physical prototype, while Fig. 4 shows the top view of the physical PCB prototype of quasi-resonant battery charger.

IV. EXPERIMENTAL RESULTS

The aim of the experimental testing was to prove the coherence of the measured open-loop operation with the theoretical analysis and extract meaningful measurements of efficiency. The experimental testbench is illustrated in Fig.

TABLE I: Main converter components for the physical prototype.

| Component	Part code	Manufacturer
MOSFETs $M_{1,6}$	TPH4R10ANLL1Q	Toshiba
Resonant inductor L_r	IHLP5050CEERR33M01	Vishay
Dividing capacitors $C_{1,2}$	C1812C944J5JLC7805	KEMET
Input capacitor C_in	UCZ1J751MNS1MS	Nichicon
Output filter inductor L_o	74437529203470	Würth Elektronik
Clamping diodes $D_{1,2}$	V8PAL45HM3_A/I	Vishay
Half-bridge gate drivers	ADUM3223WARZ	Analog Devices
Dual-output DC-DC converter	PRQ3W-Q48-D55-S	Cui Inc.
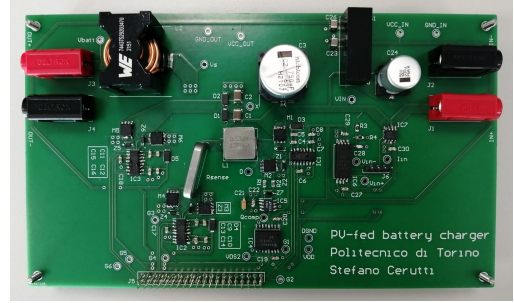
Fig. 4: Top view of the $100\,\mathrm{W}$ PCB prototype.

5. A DC power supply and a programmable electronic load were adopted as source and load, respectively. The switching functions to drive the MOSFETs were generated by Intel Cyclone V FPGA on Terasic De1-SoC board, through a Finite State Machine algorithm.

Fig. 6 shows some of the acquired experimental waveforms. Specifically, Fig. 6a depicts the steady-state behaviour of V_DS2, V_x and $i_\mathrm{L_r}$. The measurements refer to $V_\mathrm{in} = 27.5\,\mathrm{V}$, $V_\mathrm{batt} = 12\,\mathrm{V}$, $f_\mathrm{sw} = 45\,\mathrm{kHz}$ and $t_\mathrm{dead} = 80\,\mathrm{ns}$. The measured waveforms are coherent with the predicted behaviour of the converter in the DVM, since $f_\mathrm{sw} < f_\mathrm{limit} \approx 48.4\,\mathrm{kHz}$.

Fig. 6b shows a detail of the ZVS turn-ON of M_2 with the adopted deadtime value. As visible, since V_GS1 toggles to $5\,\mathrm{V}$ before $i_\mathrm{L_r}$ reverses polarity, the body diode of M_2 is conducting and ensures the zero-voltage turn-ON.

Fig. 7 reports some efficiency plots referring to different source and load voltage conditions, at a fixed $80\,\mathrm{ns}$ deadtime. The switching frequency was varied up to f_limit to modify the operating power: for each working point, the conversion
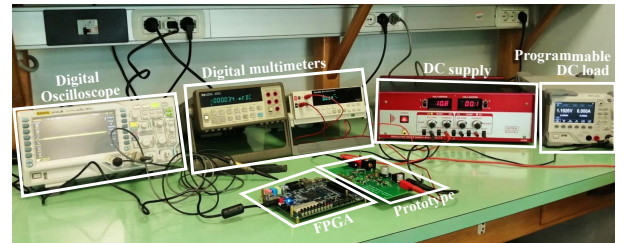

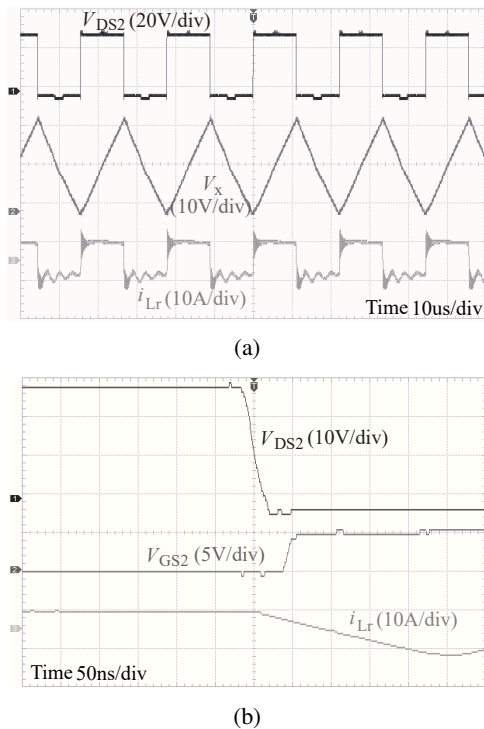Fig. 5: Testbench for the experimental validation of the prototype.

(a)

(b)

Fig. 6: Experimental waveforms of the converter: (a) V_{DS2}, V_x and i_{Lr}; (b) Zoom on V_{DS2}, V_{GS2} and i_{Lr} during the ZVS turn-ON of M_2.

efficiency was computed by including also the gate driving losses. The results show an almost flat efficiency curve independently on the source and load conditions, for operating powers larger than $20\,W$, and a peak efficiency of $94.5\,\%$. The selected deadtime ensures ZVS for almost all the power range, allowing to avoid the frequency-dependent increase of the switching losses. A flat efficiency curve is a desirable feature of PV-fed systems, due to the need to ensure high efficiency over a wide range of operating powers, intrinsic characteristic of RES. This is the reason why this converter is considered to be suitable for PV applications. At low power operations, the ZVS condition is lost and a minimum of $84\,\%$ efficiency is measured at $5\,W$.

V. CONCLUSIONS

This work proposed a new quasi-resonant battery charger designed to achieve the ZVS of its switches. The quasi-resonant behaviour exploits a small additional inductor and the parasitic capacitances of the MOSFETs, allowing to decrease the overall component count. The adoption of an active rectifier and the selection of low $R_{DS,ON}$ MOSFETs allow to decrease the conduction losses, while the ZVS minimizes the switching losses over a wide range of operating powers. A $100\,W$ prototype is designed and tested to validate the operating principle and measure the conversion efficiency. The experimental results are in agreement with the expected operation and prove that the charger is able to achieve an almost flat efficiency over the wide $20\,W - 95\,W$ operating range with
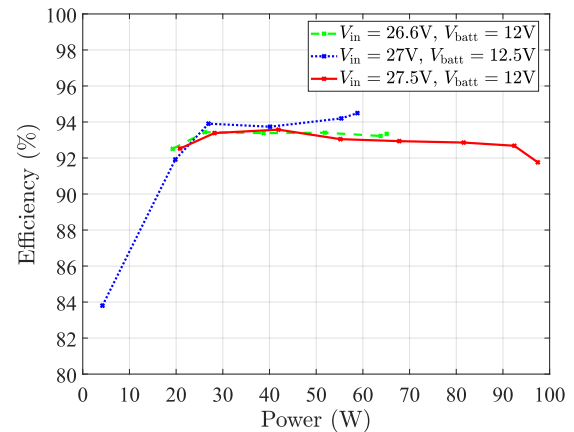

Fig. 7: Measured conversion efficiency as function of operating power, for different source and load voltages.

$94\,\%$ peak. Below $20\,W$ operation, the efficiency decreases because of the absence of ZVS condition and reaches $84\,\%$ at $5\,W$ operation.

REFERENCES

[1] J. Sachs, C. Kroll, G. Lafortune, G. Fuller, and F. Woelm, Sustainable Development Report 2022, Cambridge: Cambridge University Press, 2022.

[2] E. O. Ogunniyi and H. Pienaar, "Overview of battery energy storage system advancement for renewable (photovoltaic) energy applications," 2017 International Conference on the Domestic Use of Energy (DUE), Cape Town, South Africa, 2017, pp. 233-239, doi: 10.23919/DUE.2017.7931849.

[3] M.K. Kazimierczuk, and D. Czarkowski, Resonant Power Converters, Hoboken: Wiley, 2012.

[4] S. Kouro, J. I. Leon, D. Vinnikov and L. G. Franquelo, "Grid-Connected Photovoltaic Systems: An Overview of Recent Research and Emerging PV Converter Technology," in IEEE Ind. Electron. Mag., vol. 9, no. 1, pp. 47-61, March 2015, doi: 10.1109/MIE.2014.2376976.

[5] Y. -C. Chuang and Y. -L. Ke, "A Novel High-Efficiency Battery Charger With a Buck Zero-Voltage-Switching Resonant Converter," in IEEE Trans. Energy Convers., vol. 22, no. 4, pp. 848-854, Dec. 2007, doi: 10.1109/TEC.2006.882416.

[6] Y. -C. Chuang, "High-Efficiency ZCS Buck Converter for Rechargeable Batteries," in IEEE Trans. Ind. Electron., vol. 57, no. 7, pp. 2463-2472, July 2010, doi: 10.1109/TIE.2009.2035459.

[7] Y.-L. Ke, Y.-C. Chuang, M.-S. Kang, Y.-K.g Wu, C.-M. Lai and C.-C. Yu, "Solar power battery charger with a parallel-load resonant converter," 2011 IEEE-IAS Annu. Meet., Orlando, FL, 2011, pp. 1-8, doi: 10.1109/IAS.2011.6074300.

[8] N. K. Poon, B. M. H. Pong and C. K. Tse, "A constant-power battery charger with inherent soft switching and power factor correction," in IEEE Trans. Power Electron., vol. 18, no. 6, pp. 1262-1269, Nov. 2003, doi: 10.1109/TPEL.2003.818823.

[9] S. Chander, A. Purohit, A. Sharma, Arvind, S.P. Nehra, M.S. Dhaka, "A study on photovoltaic parameters of mono-crystalline silicon solar cell with cell temperature," Energy Reports, vol. 1, pp. 104-109, 2015, doi: 10.1016/j.egyr.2015.03.004.

[10] A. Elkhateb, N. A. Rahim, J. Selvaraj and B. W. Williams, "The effect of input current ripple on the photovoltaic panel efficiency," 2013 IEEE Conf. Clean Energy Technol. (CEAT), Langkawi, Malaysia, 2013, pp. 478-481, doi: 10.1109/CEAT.2013.6775680.

[11] S. Gerner, T. Ruhlmann, , "Effect of AC Ripple on VRLA Battery Performance", Emerson Network Power, Columbus, OH, Tech. Note TN-0008, 2010.

[12] Analog Devices Design Center - LTspice. Available: https://www.analog.com/en/design-center/design-tools-and-calculators/\ltspice-simulator.html. Accessed: Feb. 9, 2023.